NANOROBOTS

Spring-loaded DNA origami arrays as energy-supplied hardware for modular nanorobots

Martina Pfeiffer[1]†, Fiona Cole[1]†, Dongfang Wang[2,3]†, Yonggang Ke[2]*, Philip Tinnefeld[1]*

DNA origami nanorobots allow for the rational design of nanomachines that respond to environmental stimuli with preprogrammed tasks. To date, this mostly is achieved by constructing two-state switches that, upon activation, change their conformation, resulting in the performance of an operation. Their applicability is often limited to a single, specific stimulus-output combination because of their intrinsic properties as two-state systems only. This makes expanding them further challenging. Here, we addressed this limitation by introducing reconfigurable DNA origami arrays as networks of coupled two-state systems. This universal design strategy enables the integration of various operational units into any two-state system within the nanorobot, allowing it to process multiple stimuli, compute responses using multilevel Boolean logic, and execute a range of operations with controlled order, timing, and spatial position. We anticipate that this strategy will be instrumental in further developing DNA origami nanorobots for applications in various technological fields.

INTRODUCTION

Over the past decades, the DNA origami technique (*1*, *2*) has emerged as an indispensable tool for designing devices capable of emulating functions and properties of naturally occurring machines on the nanoscale and, beyond that, increasingly performing robotic tasks such as sensing, computing, and actuating (*3*–*10*). DNA origami involves the folding of a long single-stranded scaffold strand into a custom shape by up to hundreds of oligonucleotide "staple" strands. Most current DNA origami nanodevices are designed and optimized to perform a specific operation such as cargo release (*4*, *7*, *8*, *11*), a rotational motion (*3*, *12*, *13*), or a chemical reaction (*5*, *14*) after sensing chemical or physical stimuli (*15*). This is often achieved by inducing a single, relatively simple conformational change in the nanodevice, causing it to act as a two-state switch whose operation may optionally include simple AND or OR (*6*, *7*) gate logics. The conformational change alters the proximity of interacting players of the operational parts of the nanodevice, resulting in the performance of a defined operation. However, the fact that this concept is based on a single conformational change makes expanding it further challenging. Only a few examples of the realization of more sophisticated nanodevices capable of autonomously performing a series of operations in response to different combinations of environmental stimuli have been presented (*16*).

Here, we present the DNA origami nanorobot platform SEPP (serial execution of programmable processes) that uses a preexisting design for a reconfigurable DNA origami array composed of multiple, structurally similar blocks—so-called antijunctions—as the basis for multistep operations (Fig. 1, A and B) (*17*–*19*). Antijunctions are small symmetric constructs containing four DNA duplex domains of equal length that are pairwise stacked as well as four dynamic nicking points. They exist in two stable conformations with reversed stacking order between which they can switch via an unstable open conformation (*17*). In reconfigurable DNA origami arrays, multiple antijunctions are coupled to each other by the scaffold strand, which threads through the whole system. It interconnects the individual antijunctions and exerts allosteric strain to adapt the same conformation. Hybridization of fuel DNA strands to certain antijunctions at the edge of the structure stiffens those DNA regions so that the conformation of the whole system is reconfigured in a diagonal stepwise manner (Fig. 1B). In each of the steps, a row of antijunctions in the system undergoes a conformational change, ultimately resulting in the reconfiguration of the whole structure. Full reconfiguration of DNA origami arrays has previously been used to activate different proximity-induced operations (*20*, *21*), such as the onset of catalytic activity (*22*); the performance of different pattern operations involving writing, erasing, and shifting (*23*); the generation of an optical output signal (*20*); or the release of cargo DNA strands (*24*). However, a limitation of previous work is that these stimuli did not target the conformation of a specific antijunction in the system. Rather, they targeted the overall conformation of the system itself, disregarding the potential of its intermediates and reducing it to a simple two-state switch.

In contrast, SEPP interprets reconfigurable DNA origami arrays as two-dimensional networks of coupled two-state switches represented by their individual antijunctions. SEPP builds on our previous work that qualitatively uncovered the energy landscape of the reconfiguration process (Fig. 1C) (*17*, *18*, *24*) and showed how, by incorporation of energy barriers, the coupling between different antijunctions is rationally altered to retard or even fully stop the reconfiguration at a specified intermediate step (*24*). The gained mechanistic understanding changed our perspective of reconfigurable DNA origami arrays as a system of coupled nodes that provide an order of transitions, each of which can be addressed individually. Thus, the DNA origami array constitutes the molecular "hardware" analogous to an electronic programmable logic unit, such as a field-programmable gate array (*25*), of a DNA nanorobot, which can be programmed by a software framework described in this work (Fig. 1D).

With its individual antijunctions, the hardware provides a set of nodes with known connectivity given by the network's energy landscape and a defined starting point. With the prebound fuel DNA strands, the hardware also provides an energy source to create a

[1]Department of Chemistry and Center for NanoScience, Ludwig-Maximilians-Universität München, Butenandtstr. 5-13, 81377 München, Germany. [2]Wallace H. Coulter Department of Biomedical Engineering, Emory University and Georgia Institute of Technology, Atlanta, GA 30322, USA. [3]School of Biomedical Engineering and Suzhou Institute for Advanced Research, University of Science and Technology of China, Hefei 230026, China.
†These authors contributed equally to this work.
*Corresponding author. Email: philip.tinnefeld@cup.uni-muenchen.de (P.T.); yonggang.ke@emory.edu (Y.K.)

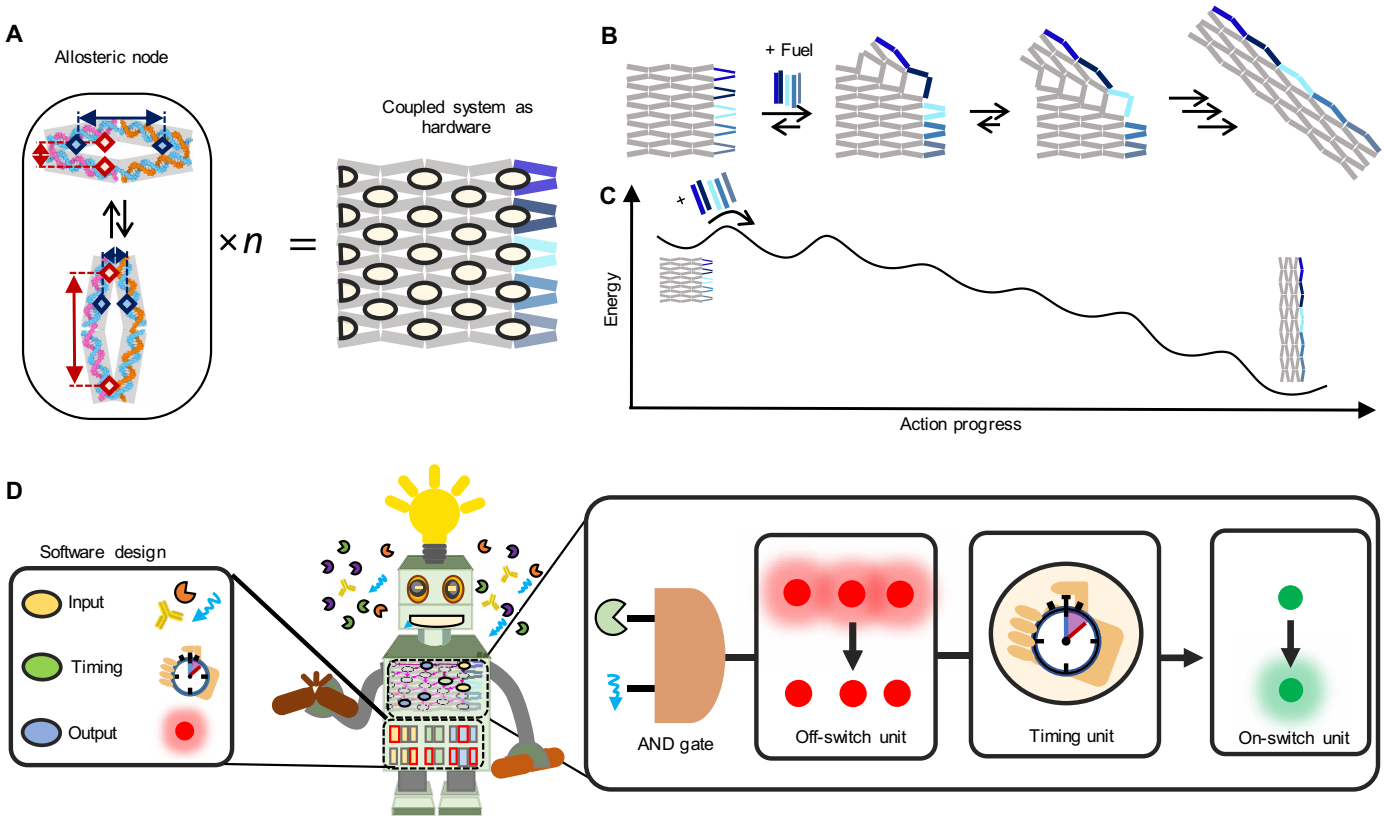

Fig. 1. Concept of a modular reconfigurable DNA origami nanorobot. (**A**) Sketch of multiple allosteric nodes coupled together in a reconfigurable DNA origami array forming the hardware of the design of the nanorobot. The nodes are indicated by ellipses at the corresponding positions in the DNA origami array. The basic unit of an allosteric node is a so-called antijunction that switches between two conformational states (left). Because of the symmetric nature of the antijunction, the switching can be used to both increase (red) and decrease (dark blue) the distance between markers placed on the antijunction depending on which domains they are placed on. (**B**) Sketch of the reconfiguration process of the unmodified DNA origami array structure occurring in a diagonal manner. Hybridization of fuel DNA strands (blue lines) to the right side of the structure yields rigid double-stranded DNA (dsDNA) instead of floppy ssDNA, exerting strain on adjacent junctions. (**C**) Simplified sketch of the previously determined energy landscape of the multistep reconfiguration process. An asymmetric design of the fuel DNA strands favors the reconfiguration beginning at the upper right corner as opposed to the bottom right corner. Higher-energy barriers in the first two steps result in time delays between these steps, whereas the more downhill-energy profile downstream results in simultaneously occurring steps on a timescale ≤200 ms (*24*). (**D**) The software modules of the designed nanorobot are formed by developing generalized strategies to encode environmental responsiveness to different targets, timings, and output operations into single allosteric nodes. The nanorobot is then formed by programming different nodes of the DNA origami array hardware with the software. This enables the robot to respond autonomously to targets in its environment in a preprogrammed, multistep manner. In the exemplary sketch shown, array transformation was activated by the presence of the green enzyme and light. Upon activation, three red fluorescence switch-off units were activated. A timing unit was then inserted to delay otherwise simultaneously occurring operations before a green fluorescence switch-on unit was activated.

spring-loaded allosteric driving force for the nanorobot's autonomous action. In our software framework, each antijunction within the system is considered as a potential input, output, or timing node. By ascribing functionality to them, the energy landscape of the transformation process is altered at the position where the corresponding node changes its conformation.

The universal and rational approach of the combined hardware and software modules was demonstrated with different inputs, such as enzyme activities, proteins, DNA, and light. The inputs were modularly combined with a range of operations, including cargo release, fluorescence on switch and off switch, and signal amplification, to achieve programmable input-output combinations (Fig. 1D). In addition, we highlight how our understanding of both the pathway and energy landscape of the reconfiguration process enables us to implement order dependencies, timing control, and multilevel logic gating as well as the simplicity of designing antagonistic operations by exploiting the antijunction's symmetric nature (Fig. 1A). As such, our molecular field-programmable gate array with software modules promises a new era of versatile nanoscale devices.

RESULTS

SEPP is based on a small reconfigurable DNA origami array structure composed of 5-by-2.5 antijunctions (five rows of 2.5 antijunctions) (*17*) that can be transformed by hybridizing five fuel DNA strands to the right side of the structure (Fig. 1, A and B, and fig. S1) (*24*). The transformation process is characterized by five intermediates (Fig. 1C). Our software framework targets the energy barriers between these intermediates and the start and end points of the transformation. To characterize SEPP at the single-molecule level with fluorescence microscopy, we incorporated dye-quencher pairs for reporting on the state of individual antijunctions and a biotinylated

single-stranded DNA (ssDNA) for surface immobilization on bovine serum albumin (BSA)–biotin/neutravidin–coated coverslips (see fig. S1 for DNA origami design and fig. S2 for characterization by gel electrophoresis and atomic force microscopy).

Design of environmentally responsive input nodes

Environmental responsiveness was encoded into the antijunction nodes by the introduction of locking units that stabilize one conformation of the targeted node over the other. This resulted in an energetic bias either hindering or favoring the transformation of the whole array (Fig. 2A). By varying the number of added fuel DNA strands, we spring-loaded the array system with varying degrees of tension and adjusted the energy levels of the untransformed and transformed states of the array to lie close together such that the presence of (multiple) locking units became the decisive factor for the transformation to occur. In the presence of the corresponding environmental input, the units were unlocked, and the energetic bias was removed, resulting in the release of the stored tension and an activation or inhibition of the transformation process. On the basis of this principle, we designed locking units responsive to ssDNA, restriction enzyme activity, light, platelet-derived growth factor BB (PDGF-BB), and antibodies (Figs. 2 and 3 and figs. S3 and S4).

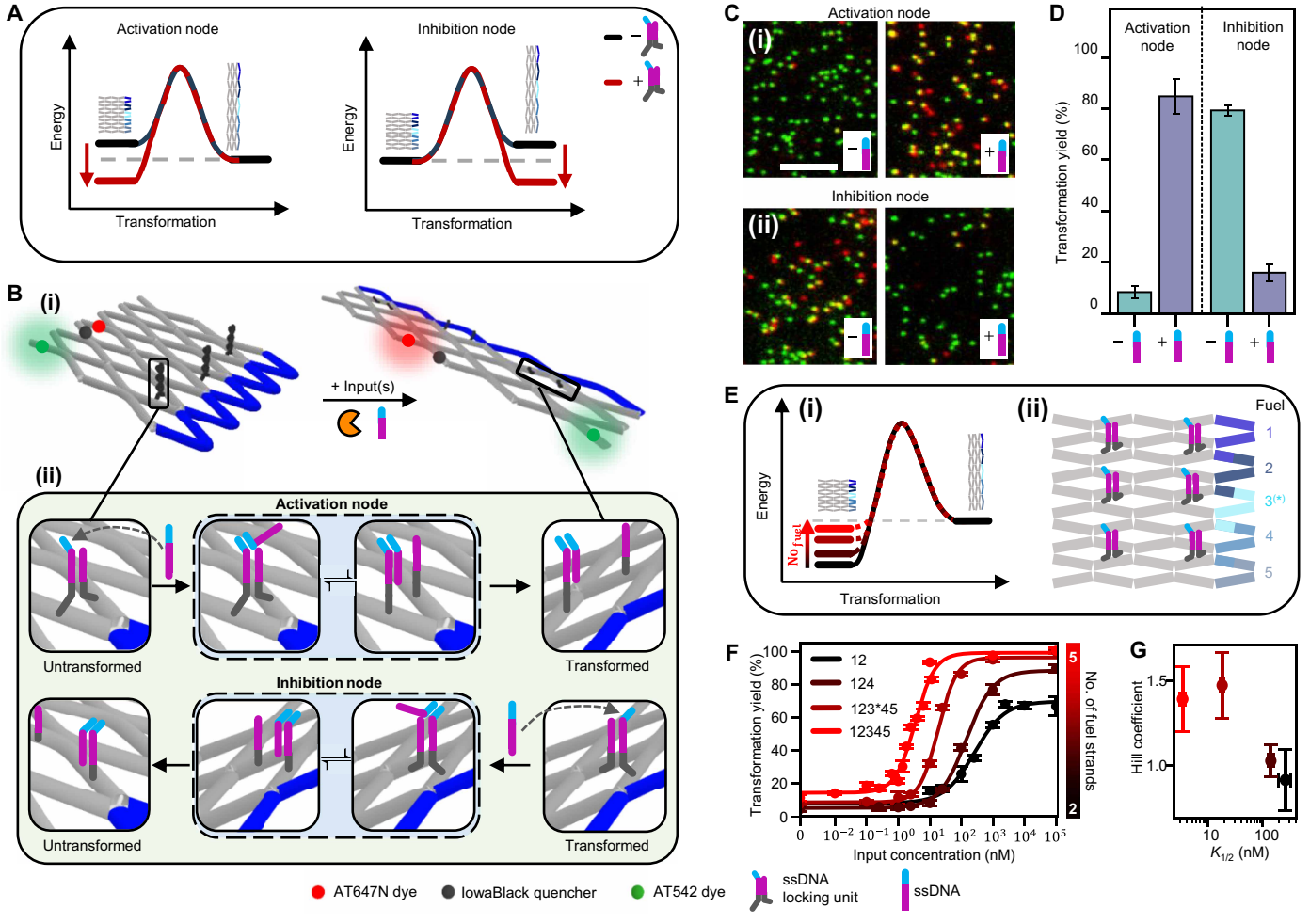

Fig. 2. Environmentally responsive activation and inhibition nodes. (**A**) Energy schemes showing the influence of a locking unit in activation and inhibition nodes on the transformation process. In the presence of their inputs, this effect is nullified. The energy schemes in the absence of the locking units are programmed priorly by adding different combinations of fuel DNA strands. (**B**) Sketch of the DNA origami nanorobot bearing environmentally responsive nodes. A red dye-quencher fluorescence resonance energy transfer (FRET) pair (ATTO 647N, IowaBlackRQ) reports on the state of the nanorobot, and a green dye (ATTO 542) is used to identify the nanorobot's position in single-molecule experiments. (i). Nodes responsive to ssDNA activating and inhibiting the transformation are based on a reversible dsDNA lock that is unlocked via a toehold-mediated strand displacement reaction with a ssDNA input (ii). (**C**) Exemplary TIRF images of DNA origami nanorobots bearing ssDNA-responsive activation (i) and inhibition (ii) nodes after incubation with fuel DNA strands 1 and 2 and strands 1 and 3*, respectively, and without or with the ssDNA input. Fuel strand 3* represents a shortened version of fuel strand 3 with only 25 nt (nucleotides) instead of 65 nt. Scale bar, 4 μm. (**D**) Corresponding transformation yields. (**E**) Strategy for tuning the responsive concentration window of the ssDNA input. (i) Increasing the number of added fuel DNA strands increases the tension in the spring-loaded system, resulting in a destabilization of the untransformed state of the array. (ii) DNA array system with six ssDNA locking units incorporated. The hybridization positions of fuel strands 1 to 5 are marked with color. (**F**) Increasing the number of added fuel DNA strands from strands 1 and 2 over 1, 2, and 4 and 1, 2, 3*, 4, and 5 to 1, 2, 3, 4, and 5 shifts the responsive window. (**G**) Influence of the number of added fuel DNA strands on $K_{1/2}$ and the Hill coefficient. Error bars in (D) and (F) represent the 95% confidence intervals in the transformation yields calculated from at least three TIRF images. Error bars in (G) represent the fit errors to the curves fitted in (F).

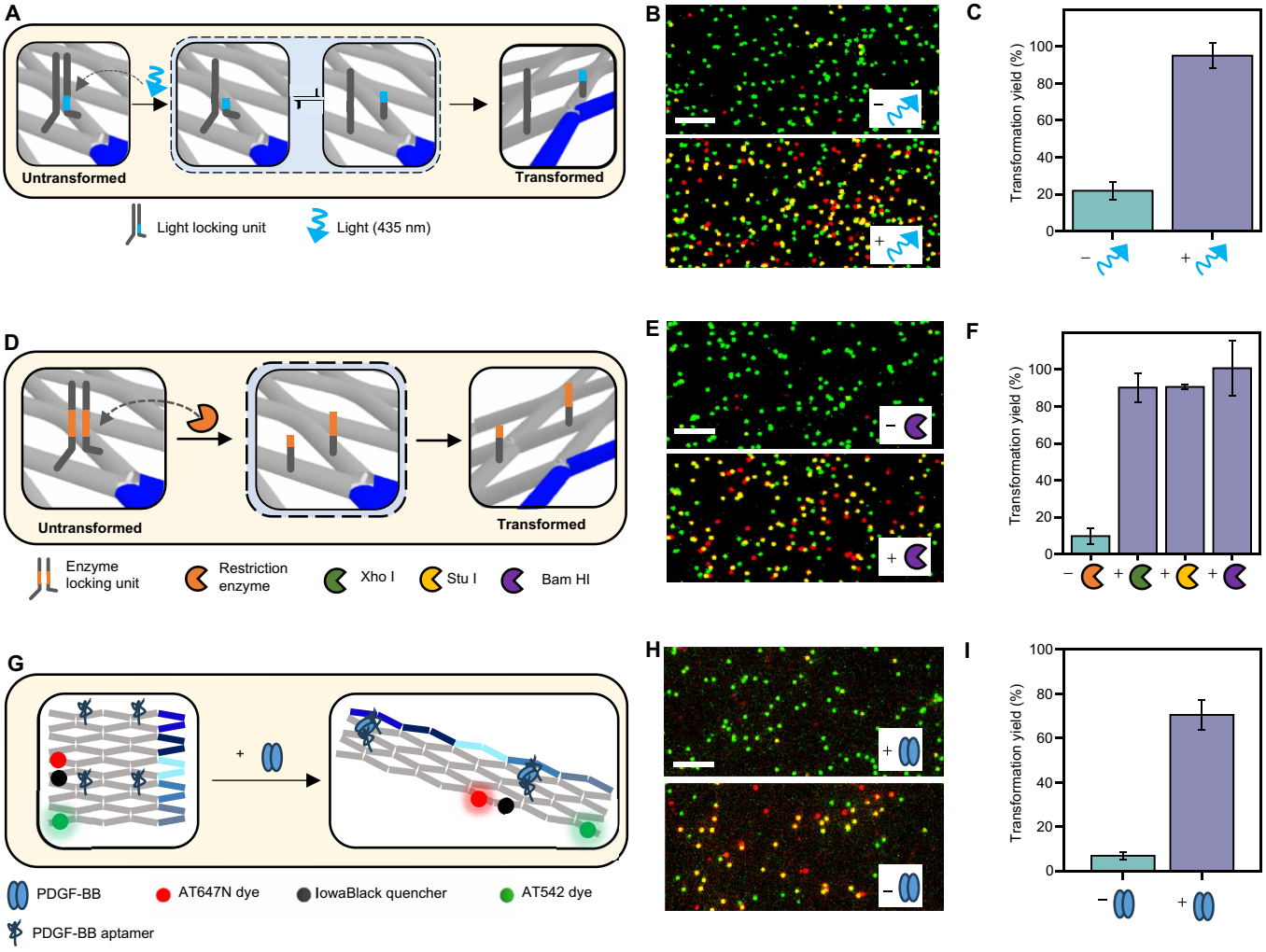

Fig. 3. SEPP response to light, enzymes, and a nonenzymatic protein. (**A**) Sketch of nodes responsive to light. The design is based on a dsDNA lock containing a light-cleavable linker. (**B**) Exemplary TIRF images of DNA origami array structures with the light-cleavable locking unit and an additional stabilization unit that stabilizes the untransformed state of the array and does not interact with any inputs incubated with fuel DNA strands 1 to 5 in the presence and absence of light. (**C**) Corresponding transformation yields. (**D** to **F**) Restriction enzyme activity as input. (D) Sketch of nodes responsive to restriction enzyme activity. Their design is based on a dsDNA lock containing the restriction enzyme–specific cleavage site. The lock is cleaved in the presence of an active restriction enzyme. (E) Exemplary TIRF images of DNA origami array structures with three restriction enzyme locking units containing the cleavage site for Bam HI before and after incubation with DNA fuel strands and after incubation with fuel strands and Bam HI. (F) Transformation yields of DNA origami array structures with three restriction enzyme locking units containing the cleavage site for Bam HI, Stu I, or Xho I before and after incubation with DNA fuel strands and Bam HI, Stu I, or Xho I. (**G** to **I**) Protein-induced transformation. (G) Sketch of nodes responsive to protein (PDGF-BB) binding. As PDGF-BB binds two aptamers, binding induces transformation. (H) Exemplary TIRF images of DNA origami array structures with two PDGF-BB–binding units, each composed of two aptamers protruding from the origami surface as indicated in the sketch, in the presence and absence of PDGF-BB, indicating the protein-induced transformation. (I) Transformation yields in the presence and absence of PDGF-BB. In addition to the inputs, light- and enzyme-responsive origami arrays were incubated with fuel DNA strands 1 to 5. The PDGF-BB–responsive origami array was incubated with fuel DNA strands 1 and 4. Error bars represent the 95% confidence intervals in the transformation yields calculated from three TIRF images. Scale bars in (B), (E), and (H), 4 μm.

For ssDNA as an input, locking units were formed by two ssDNA strands protruding from two domains of the targeted antijunction nodes. The ssDNA strands contained a complementary section that hybridized when both domains were in close proximity. Depending on which domains they were placed on, hybridization of the strands occurred in either the untransformed or transformed conformation of the nodes (Fig. 2B), resulting in their energetic stabilization. To enable unlocking, one of the protruding ssDNA strands was designed with a toehold overhang. This allowed for unlocking by toehold-mediated strand displacement with a ssDNA input.

The successful implementation of the ssDNA locking units was verified using a fluorescence onset unit placed on an antijunction node downstream in the transformation process. The fluorescence onset unit reported on the conformational state of the node it was placed on (Fig. 2B). It was based on a red dye-quencher probe (ATTO 647N, Iowa Black RQ) positioned on two different domains of an antijunction node that were in close proximity in the untransformed state of the antijunction node. The increase in distance between these domains caused by the transformation of the corresponding node resulted in an increased fluorescence signal of the dye molecule.

This allowed us to distinguish the untransformed state from the transformed state of the node. We additionally incorporated an ATTO 542 dye into the arrays and quantified the fraction of arrays in their transformed state (transformation yield) from dual-color single-molecule total internal reflection fluorescence (TIRF) images of surface-immobilized array structures collected in the absence and presence of the ssDNA input (Fig. 2C and Materials and Methods).

With a transformation yield of 10%, arrays with three ssDNA activation nodes incorporated and fuel DNA strands 1 and 2 were predominantly in their untransformed state in the absence of ssDNA input. Upon addition of ssDNA input, the arrays transformed, resulting in a transformation yield of 83%. In contrast, arrays with three ssDNA inhibition nodes incorporated and fuel DNA strands 1 and 3* showed transformation yields of 80 and 16% in the absence and presence of ssDNA input, respectively, demonstrating the antagonistic usability of the same DNA locking unit with near-quantitative responses (Fig. 2D). Because this process was reversible (fig. S5), our control over the energy landscape of the system provided additional access to tune the location ($K_{1/2}$) and width of the responsive concentration window toward the ssDNA input without modifying the ssDNA locking unit itself. When incorporating six ssDNA activation units into the array, increasing the number of added fuel DNA strands from two to five led to an increased mechanical strain exerted on the untransformed conformation of the array (Fig. 2E). This resulted in a more than 75-fold decrease in $K_{1/2}$ (from 260 ± 60 to 3.4 ± 0.4 nM) while simultaneously increasing the Hill coefficient from 0.9 ± 0.2 to 1.4 ± 0.2 and thus narrowing the responsive concentration window (Fig. 2, F and G). Reducing the number of incorporated ssDNA activation units and replacing one of the ssDNA activation units with different units introduced additional tuning strategies for the responsive window and allowed shifting $K_{1/2}$ down to 0.08 ± 0.02 nM (inhibition unit as the sixth unit; fig. S6). In combination, all strategies allowed shifting $K_{1/2}$ more than 3000-fold without modifying the ssDNA locking unit itself (*6*). This promises good adaptability of these tuning strategies toward other inputs without the need for reengineering the input-responsive locking units to create different affinities toward the inputs.

We then demonstrated the simple adaptability of our universal design approach toward other inputs. The designs of input nodes responsive to restriction enzyme activity and light were based on ssDNA locking units containing an enzyme-specific restriction site and a photocleavable linker, respectively. The locks were cleaved in the presence of an active restriction enzyme or light of a specified wavelength, effectively unlocking them (Fig. 3, A and D). When implemented as activation nodes in DNA array systems, they responded specifically to their respective inputs (Xho I, Stu I, and Bam HI restriction enzymes and light at 365 nm) by transforming quantitatively only in their presence (Fig. 3, A to F, and fig. S3) after addition of fuel DNA strands, which can also be preloaded onto the structure (fig. S7). We further extended SEPP's spectrum of inputs to nonenzymatic proteins. We designed an input unit responsive to PDGF-BB (*26*), which is a homodimeric protein associated with cancer and other diseases (*27*), and demonstrated its application in activation nodes (Fig. 3, G to I). In addition, we designed an input unit responsive to immunoglobulin G antibodies and demonstrated its application in inhibition nodes (fig. S4).

Computation based on Boolean logic

In the design of our locking units, the presence of a single unit alone did not suffice to quantitatively initiate or inhibit the transformation process when the arrays were spring-loaded with all five fuel DNA strands (Supplementary Discussion and fig. S8). This design anticipated the rational creation of computation schemes, thus providing the ability to respond to diverse input combinations in a preprogrammed manner. We systematically characterized the influence of restriction enzyme locking units positioned at different nodes, both individually and in combinations (Fig. 4A and fig. S8). Notably, when comparing the effects of the same locking unit positioned at two different nodes in an otherwise identical design, we observed substantial differences in the obtained transformation yields (Fig. 4A). When the locking unit was positioned at a node transforming during the first step of the transformation process, the transformation was inhibited. In contrast, placing the unit at a node transforming during the fourth step resulted in an increased transformation yield of 70%. This finding aligned with the qualitative profile of the energy landscape of the transformation process and was also consistent with all other studied locking unit combinations (Supplementary Discussion and fig. S8). The tilted profile of the energy landscape indicates a weakened effect of an incorporated locking unit the further downstream the corresponding antijunction node is in the transformation cascade. Using this dependence and placing multiple locking units specific to various inputs at predefined antijunction nodes on the same structure, we established a computation framework to program responses to diverse input combinations based on Boolean logic gates.

We first implemented basic Boolean AND and OR gates responsive to combinations of the restriction enzymes Xho I and Stu I. We again used a fluorescence switch-on unit to confirm the designed responsiveness of the system. For the AND gate, a near-quantitative transformation occurred (Fig. 4B and fig. S9) only upon addition of both restriction enzymes, whereas for the OR gate, the addition of one restriction enzyme resulted in transformation yields of above 80% (Fig. 4C and fig. S9). The applicability of these gates was not limited to inputs of the same molecular class. Our modular design strategy of locking units, for example, allowed the simple exchange of the Xho I locking unit with a light locking unit in the OR gate design while maintaining the functionality of the gate (Fig. 4D and fig. S9). This demonstrated how inputs of different molecular classes can be processed on the same structure in DNA origami arrays using SEPP.

Both the AND and OR gate designs demonstrated low leakages in all logical FALSE conditions, with the TRUE state providing at least fourfold higher transformation yields in all cases. The low leakages of these basic gates allowed expanding the concept further to include multilevel logic gates. We used the multistep nature of the transformation cascade to (figuratively speaking) create cascades of multiple logic gates and connect them in series. Using the prior characterization of the effect of restriction enzyme locking units at different positions as a basis, we designed two multilevel logic gates of different complexities: a 3× AND gate that was composed of two logic AND gates connected in series (Fig. 4E and fig. S10) and a gate that only gave a positive response if at least two of its three inputs were present (fig. S11). We found that both systems provided low leakages in all logical FALSE conditions that were statistically distinguishable from the transformation yields obtained for the TRUE states, demonstrating the successful implementation of the designed gates. Besides logic gating, SEPP's modularity enabled multiplexing as an additional pathway to process multiple inputs in parallel (fig. S12).

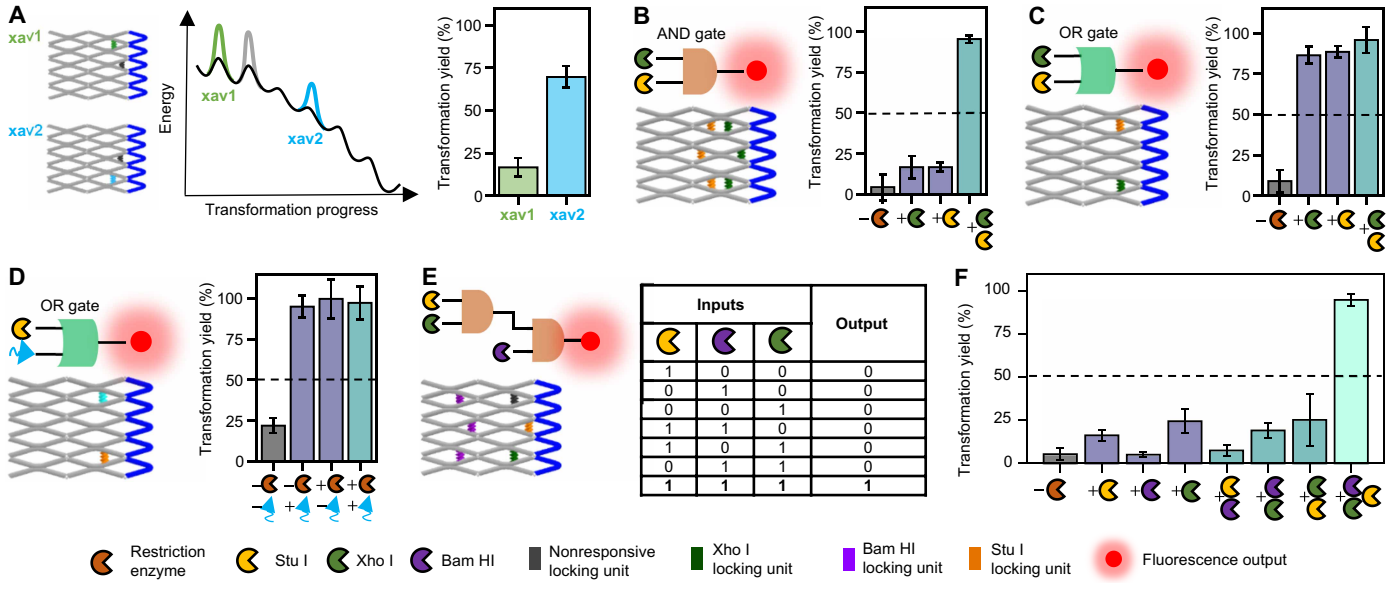

Inputs			Output
1	0	0	0
0	1	0	0
0	0	1	0
1	1	0	0
1	0	1	0
0	1	1	0
1	**1**	**1**	**1**

Fig. 4. DNA origami array nanorobot processing one- and multilevel Boolean logic gates. One-level and multilevel Boolean logic gates responsive to combinations of restriction enzymes and light were implemented by combining different restriction enzyme/light locking units and stabilization units. The molecular logic was programmed by the number and position of the incorporated units. In addition, a red fluorescence onset unit was incorporated for reading out the state of the robot. (**A**) Comparison of the transformation yields of two array designs. The designs differ only in the position of one locking unit stabilizing the untransformed conformation marked in green (xav1) and blue (xav2) that targets different positions in the energy landscape of the transformation process. The gray locking unit/energy barrier was present in both designs. (**B**) Schematic design of a basic logic AND gate responsive to combinations of Xho I and Stu I and obtained transformation yields. (**C**) Schematic design of a basic logic OR gate responsive to combinations of Xho I and Stu I and obtained transformation yields. (**D**) Schematic design of a basic logic OR gate responsive to combinations of Stu I and light and obtained transformation yields. (**E**) Schematic design of a 3× AND gate and (**F**) obtained transformation yields. In addition to possible inputs, all DNA origami arrays were incubated with fuel DNA strands 1 to 5. Error bars represent the 95% confidence intervals in the transformation yields calculated from three TIRF images.

Combining logical gated input operations with output operations

The aim of smart nanorobots includes not only programming responses to different input combinations but also the conduction of these responses if the required conditions are met. Beyond simple fluorescence onset units to generate output signals, we next demonstrated different output operations and combined input-responsive locking units with a more complex output operation. As an example, we chose a cargo release unit, which upon activation released a fluorescently labeled (ATTO 542) cargo DNA strand from the system (Fig. 5A and Supplementary Discussion) (*24*).

First, we combined the cargo release unit with restriction enzyme locking units specific to the activity of Bam HI. Here, the fraction of structures carrying a DNA cargo strand was determined from the colocalization yield with an ATTO 647N dye additionally incorporated in the DNA origami.

After assembly, DNA origami arrays near-quantitatively carried the cargo DNA strand (fig. S13). Upon incubation with and without an enzyme, the fraction of structures carrying the cargo dropped from 98% to 20 and 75%, respectively (Fig. 5, B to D). Although this indicated some unspecific cargo release, most cargo was only released in the presence of the restriction enzyme. We attributed the unspecific loss of the cargo strand to the decreased stability at the incubation temperature of 37°C (Supplementary Discussion and fig. S13). Given that we achieved both the implementation of logic gates and variable input-output combinations, we then used the modularity of our system to combine all of the above. We designed structures that compute the controlled release of cargo in response to combinations of Xho I and Bam HI activity. In both AND and OR logic configurations, a high fraction of cargo was released only when the gate gave a positive response (Fig. 5, E and F, and figs. S14 and S15).

Constructing networks of multiple inputs and outputs

Analogous to the input units, SEPP also enabled incorporating multiple output units. This can be used to amplify these outputs as we demonstrated exemplarily for the fluorescence onset unit (fig. S16) or to perform different events consecutively (fig. S17). Here, we used previously developed timing units based on a DNA lock to control order and timing between different events (*24*, *28*). Timing units slightly heighten the activation barrier at a certain intermediate step in the transformation cascade and thus introduce a time lag between operations placed on antijunctions transforming before and after them. We demonstrated this exemplarily by positioning a timing unit between two fluorescence switch-on units. In the absence of the timing unit, the fluorescence switch-on units lit up simultaneously upon activation by restriction enzyme activity. If a timing unit was incorporated, a time lag between both fluorescence onsets was achieved for most structures. The order in which the fluorescence onset units lit up could be reversed by switching the antijunction nodes they were incorporated in (fig. S17).

We then set out to make full use of our designed software framework and combined all developed unit types in a single system using ssDNA and restriction enzyme input units, fluorescence switch-on and switch-off output units (fig. S18), and a timing unit (Fig. 6A). In the absence of inputs, SEPP showed only a red fluorescence signal (Fig. 6, B and C). Upon activation by a ssDNA input and Xho I

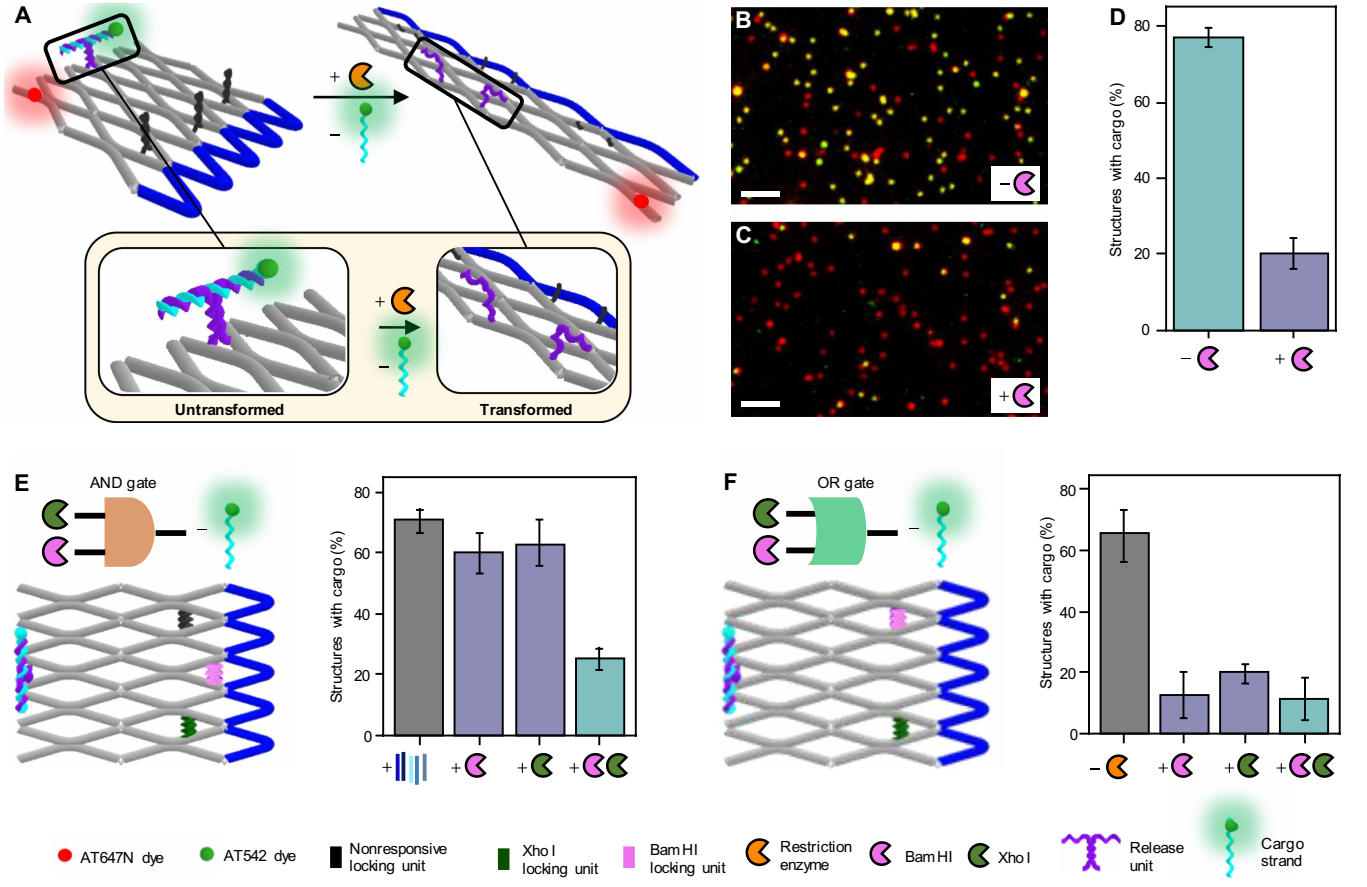

Fig. 5. Proximity-induced output operation generated upon molecular inputs by a DNA origami array nanorobot. (**A**) Schematic representations of DNA origami array structures that release a cargo DNA strand in response to the activity of Bam HI. (**B** and **C**) TIRF images of the DNA origami array nanodevice after incubation (B) without and (C) with Bam HI. Scale bar, 3 μm. (**D**) Corresponding fractions of DNA origami array nanodevices with a bound cargo DNA strand. (**E** and **F**) Schematic representations of DNA origami array nanodevices computing the controlled release of a cargo in response to the presence of combinations of Xho I and Bam HI and corresponding fractions of DNA origami array nanodevices with a bound cargo DNA strand for AND (E) and OR (F) logic gates. In addition to possible inputs, all DNA origami arrays were incubated with fuel DNA strands 1 to 5. Error bars represent the 95% confidence intervals of the fractions calculated from three TIRF images.

restriction enzyme activity combined to a logic AND gate, SEPP switched off the red fluorescent signal (Fig. 6, B and C). Depending on whether an additional timing unit was incorporated or not, a green fluorescent signal lit up either after the red fluorescence offset occurred or simultaneously with it (Fig. 6, B to G). This good agreement between the programmed function and execution exemplified the control achievable in programmed systems using SEPP.

DISCUSSION

We demonstrated the rational development of DNA origami nanorobots using the network of coupled two-state systems offered by DNA origami arrays as a programmable hardware and fuel DNA strands as an energy source that spring-load the system with varying degrees of tension. By designing a software package that defines different units, we showed how a wide range of functionalities can be encoded into any of the network's two-state systems and connected through the network's energy landscape. We designed input units responsive to ssDNA, light, restriction enzyme activity, and nonenzymatic proteins that either activated or inhibited the DNA origami array transformation. By combining multiple units on a single DNA array structure, we developed strategies to tune the responsive input concentration window, shifting $K_{1/2}$ more than 3000-fold and controlling cooperative behavior. We used the same strategy to incorporate Boolean logic gating, creating specific responses for different input combinations, with inputs of the same and different molecular classes. Subsequently, we demonstrated the potential of the modularity of this software-hardware combination. We programmed a nanorobot that combined activation by different inputs with Boolean logic gating and a sequence of output operations, such as (amplified) fluorescence output or cargo release, conducted in a predefined order and under temporal control and demonstrated its proper functionality.

The easy integration of many different functionalities and molecule classes was based on the allosteric strain as the driving force that distinguishes the approach from common strand displacement–driven DNA computing and robotics approaches. This also enabled autonomous functionality without an external energy supply for every step (*6*). For further upscaling of the approach, larger DNA origami array structures have to be used, and the sequence design controlling the energy landscape will have to be optimized so that operations are still reliable when the locking/unlocking units are farther away from the fuel strands. Alternatively, cascading could be achieved by passing cargo to the next DNA origami array by diffusion.

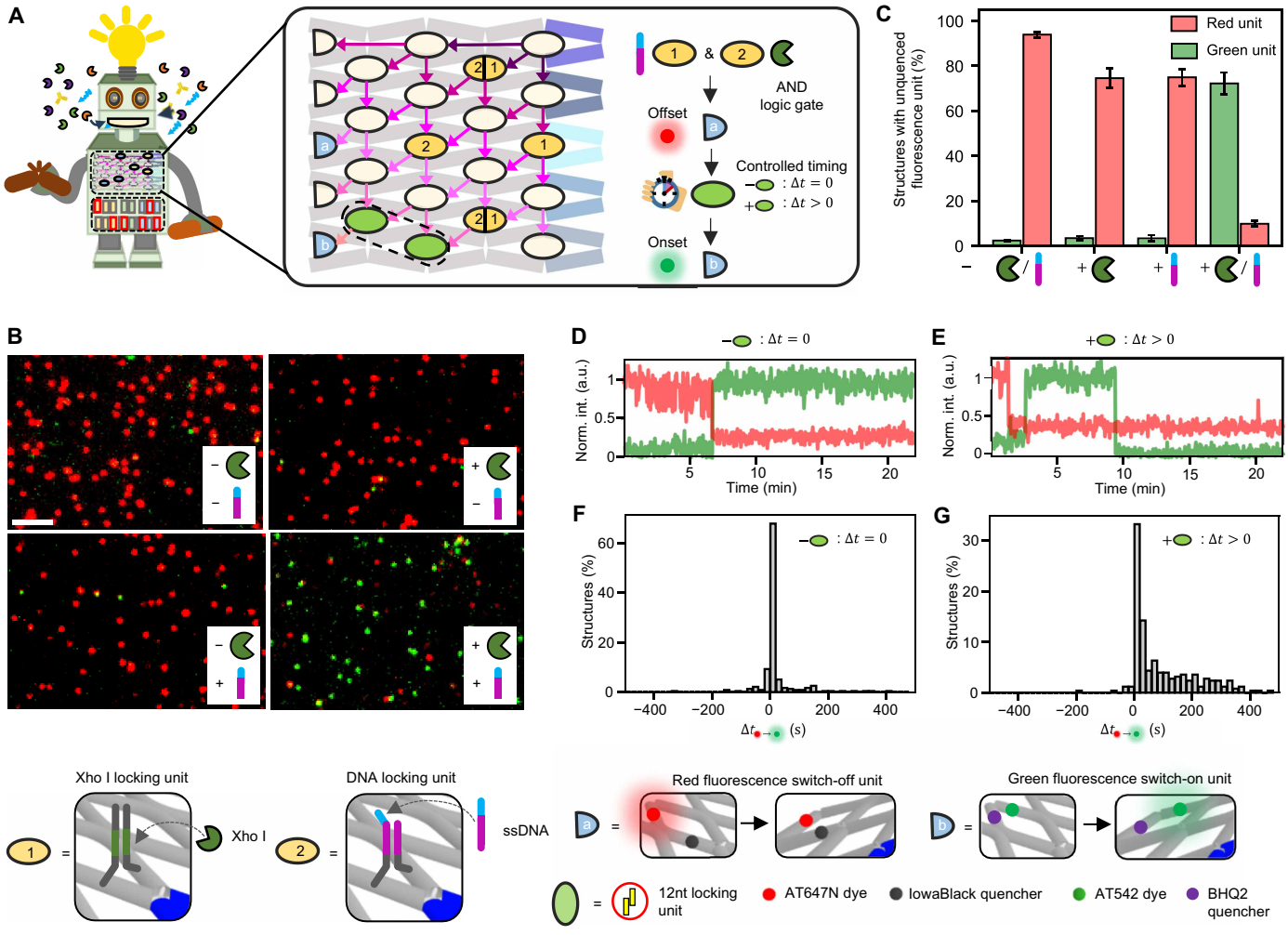

Fig. 6. Programming a DNA origami array nanorobot. The nanorobot performs output operations under temporal control after processing a Boolean logic AND gate on the basis of restriction enzyme activity and ssDNA binding. (**A**) Schematic design of a DNA origami array nanorobot programmed to perform a series of operations with the corresponding plan of action. (**B**) TIRF images of the DNA origami array nanorobot after incubation with different combinations of restriction enzyme and/or ssDNA. Scale bar, 3 μm. (**C**) Corresponding fractions of structures with unquenched green and red fluorescence units. Error bars represent the 95% confidence interval in the fractions calculated from three TIRF images. (**D** and **E**) Exemplary single-molecule transients for structures without (D) and with (E) a timing unit incorporated. In (E), photobleaching is responsible for the sudden drop of green emission after ~9 s. a.u., arbitrary units. (**F** and **G**) Time between the occurrence of the red fluorescence offset and the green fluorescence onset for structures without (F) and with (G) a timing unit incorporated. In addition to possible inputs, all DNA origami arrays were incubated with fuel DNA strands 1 to 5.

Overall, we expect that expanding our hardware with different DNA origami arrays and software packages with further proximity-based operations will be straightforward. Including further input and output software units that (besides the demonstrated cargo release and fluorescence on/offset) enable, e.g., the on-demand onset of catalysis or cargo uptake (*22*), will pave the way for a broad range of applications in clinical diagnostics. Implementation of arising DNA origami stabilization strategies that have to be tested with respect to their compatibility with reconfigurable DNA origami arrays (*29*–*31*) could also extend this approach to therapeutics.

MATERIALS AND METHODS

Synthesis of DNA origami arrays

DNA origami structures were designed using the open-source software caDNAno2 (*32*) and assembled and purified using published protocols (*33*). For the exact sequences of all unmodified and modified DNA staple strands used to fold the DNA origami structures, see tables S1 to S11. DNA staple strands were purchased from Eurofins Genomics GmbH (Germany) and Integrated DNA Technologies (USA).

For DNA origami folding, 10 nM in house–produced p1800 scaffold in 1× TAE (400 mM tris, 400 mM acetic acid, and 10 mM EDTA, pH 8) containing 12.5 mM $MgCl_2$ was mixed with a 10-fold excess of all unmodified oligonucleotides and a 30-fold excess of all modified oligonucleotides. The mixture was heated to 65°C in a thermocycler and kept at this temperature for 15 min before being cooled down to 25°C with a temperature gradient of −1°C/min. Folded DNA origamis were purified from excessive staple strands by gel electrophoresis. All gels were run using a 1.5% agarose gel and 1× TAE containing 12.5 mM $MgCl_2$ for 2 hours at 6 V/cm. The target band containing DNA origami was cut from the gel, and the DNA origami solution was extracted from the band via squeezing.

Sample preparation on the coverslip for single-molecule wide-field measurements

For chamber preparation, adhesive SecureSeal hybridization chambers (2.6-mm depth, Grace Bio-Labs, USA) were glued on microscope coverslips with a 24 mm–by–60 mm area and 170-μm thickness (Carl Roth GmbH, Germany). The created wells were incubated with 1 M KOH for 1 hour and washed three times with 1× phosphate-buffered saline (PBS) buffer. After surface passivation by incubation with BSA-biotin (0.5 mg/ml; Sigma-Aldrich, USA) for 10 min, the surface was washed with 200 μl of 1× PBS buffer. One hundred fifty microliters of neutravidin (0.25 mg/ml; Thermo Fisher Scientific, USA) was incubated for 10 min and then washed three times with 150 μl of 1× PBS buffer. Surface immobilization was achieved via biotin-neutravidin interactions. For this, we incorporated one biotinylated DNA staple strand in the loop of the DNA origami structure during folding. The DNA origami solution was diluted with 1× tris-EDTA (TE) buffer containing 750 mM NaCl to a concentration of ~10 pM and then immobilized on the biotin-neutravidin surface via biotin-neutravidin interactions. For this, 150 μl of the DNA origami sample solution was added and incubated for 5 min. The residual unbound DNA origami was removed by washing the chambers with 150 μl of 1× TE buffer containing 750 mM NaCl. The density of DNA origami on the surface suitable for single-molecule measurements was checked on a TIRF microscope. If required, the density of DNA origami was increased by repeating the incubation with a DNA origami solution with a higher concentration of ~20 pM. For acquisition of single-molecule fluorescence movies, an oxidizing and reducing buffer system (1× TAE, 12.5 mM $MgCl_2$, and 2 mM Trolox/Troloxquinone) (*34*) was used in combination with an oxygen scavenging system (12 mM protocatechuic acid, 56 μM protocatechuate 3,4-dioxygenase from *Pseudomonas* spp., 1% glycerol, 1 mM KCl, 2 mM tris-HCl, and 20 μM EDTA-$Na_2{\cdot}2H_2O$) to suppress blinking and photobleaching. For this, protocatechuic acid was added to the oxidizing and reducing buffer system. This combined buffer solution then was added to the measurement chamber. Directly before starting the measurement, procatechuate 3,4-dioxygenase was added from a 50× stock. The chamber was sealed. If not stated otherwise, for acquisition of single TIRF images, no oxidizing and reducing buffer system was added.

Reconfiguration of DNA origami array structures in response to different molecular inputs

ssDNA detection assay

For the detection of ssDNA, DNA origami array structures were folded with ssDNA locking units. After surface immobilization, 50 nM fuel DNA strands in 1× TE buffer containing 750 mM NaCl and, if not stated otherwise, 2 μM ssDNA input were added. The samples were incubated at 37°C for 15 min, and dual-color TIRF images were recorded. For titration curve measurements, samples were incubated overnight to ensure equilibrium conditions.

Restriction enzyme activity assay

For the detection of restriction enzyme activity, DNA origami array structures were folded with restriction enzyme locking units. All five fuel DNA strands (50 nM) in 1× TAE buffer containing 12.5 mM $MgCl_2$ and 2 μl of Xho I (20,000 units/ml, New England BioLabs, USA), Stu I (10,000 units/ml, New England BioLabs, USA), or Bam HI (100,000 units/ml, New England BioLabs, USA) were added to surface-immobilized DNA origami samples. To determine transformation yields, the structures were incubated for 15 min at 37°C, and dual-color TIRF images were recorded. To measure transformation time distributions (e.g., for the incorporation of timing units), sample chambers were sealed immediately after addition of the enzymes, and the photostabilization system and dual-color movies of the DNA origami arrays were acquired for 20 min at 37°C.

Light detection assay

For the detection of light at 365 nm, DNA origami structures were folded with a light-responsive locking unit. All five fuel DNA strands (50 nM) in 1× TAE buffer containing 12.5 mM $MgCl_2$ were added to surface-immobilized DNA origami samples, and the samples were illuminated with light at 365 nm for 5 min. After subsequent incubation at 37°C for 15 min, dual-color TIRF images were recorded.

Anti-DIG antibody detection assay

For the detection of anti–digoxigenin (DIG) antibodies, DNA origami array structures were folded with two DIG recognition elements. Fuel DNA strands 1 and 2 (50 nM) in 1× TE buffer containing 750 mM NaCl and 100 nM anti-DIG antibodies (Rb Monoclonal, Thermo Fisher Scientific, cat. no. 700772, PRID: AB_2532342) were added to surface-immobilized DNA origami samples. Samples were incubated at 37°C for 15 min, and dual-color TIRF images were recorded.

PDGF detection assay

For the detection of PDGF-BB, DNA origami arrays were folded with four PDGF-BB aptamers. Fuel DNA strands 1 and 4 (50 nM) in 1× TAE buffer containing 12.5 mM $MgCl_2$, 1% BSA, and 10 nM recombinant human PDGF-BB (Peprotech) were added to surface-immobilized DNA origami samples. Samples were incubated at 37°C for 2 hours, and dual-color TIRF images were recorded.

Boolean logic gating and cargo release assays

For the measurement of Boolean logic gates and cargo release, surface-immobilized DNA origami structures were incubated with 50 nM fuel DNA strands 1 to 5 in 1× TAE buffer containing 12.5 mM $MgCl_2$ and the different restriction enzyme or light inputs at 37°C as described above, and dual-color TIRF images were recorded.

Nanorobot measurement combining multiple inputs with multiple outputs

For the nanorobot measurement that combined multiple inputs with multiple outputs (Fig. 5), surface-immobilized DNA origami array structures were incubated with 50 nM fuel DNA strands 1 to 5 in 1× TAE buffer containing 12.5 mM $MgCl_2$ and different combinations of 2 μl of Bam HI/2 μM ssDNA at 37°C, as described above. For determining the fraction of structures with unquenched fluorescent units, dual-color TIRF images were recorded after 15 min of incubation time. For determining the time delay between the red fluorescence offset and the green fluorescence onset, sample chambers were sealed immediately after addition of both inputs, and the photostabilization system and dual-color movies of the DNA origami arrays were acquired for 20 min at 37°C.

Wide-field measurements

For the detection of single-molecule fluorescence, a commercial wide-field/TIRF microscope Nanoimager from Oxford Nanoimaging Ltd. was used. Red excitation at 638 nm was realized with a 1100-mW laser, and green excitation at 532 nm was realized with a 1000-mW laser. The relative laser intensities were set to 9% for green excitation and to 18% for red excitation. The microscope was set to TIRF illumination. Measurements were carried out at 37°C. For quantifying transformation yields and the percentage of structures carrying cargo, dual-color fluorescence images were acquired. For recording

fluorescence movies, the lasers were activated, and a frame of 100 ms was taken every second separately for both excitation lasers (with a time lag of 0.5 s between them) over a measurement period of 20 min.

Data analysis

We quantified the percentage of transformed structures by dividing the number of green (ATTO 542) and red (ATTO 647N) colocalized spots by the total number of green spots from dual-color TIRF images. To account for a labeling efficiency <100%, the percentage of colocalized spots was normalized by the percentage of colocalized spots of a DNA origami array folded with all five fuel DNA strands to calculate transformation yields. In the normalization sample, atomic force microscopy imaging confirmed the full transformation of all structures in previous work (*24*). For structures with a cargo release unit incorporated, the percentage of structures carrying cargo was determined analogously.

Data processing and analysis of time-lapse movies were realized using custom-written Python scripts. Briefly, the acquired movies were first drift-corrected using DNA origami structures carrying fluorophores that were in their fluorescent state throughout the whole measurement as fiducial markers. Spots appearing during the measurement were detected from the drift-corrected movies, and dual-color background-subtracted fluorescence intensity transients of those spots were extracted. To determine transformation times of single structures, the corresponding transients were fitted using a hidden Markov model. Two levels corresponding to the quenched and unquenched states of the corresponding fluorescence unit were defined. For fluorescence switch-on (switch-off) units, transformation times were defined as the time a structure switches from its quenched (unquenched) state to its unquenched (quenched) state and subsequently remains in it for at least 10 s for the first time. To determine transformation time distributions, only structures showing an intensity change in both colors were considered.

For titration curve measurements, the transformation yields obtained upon incubation with different concentrations of ssDNA input [DNA] were calculated from dual-color TIRF images, as described above. $K_{1/2}$ and the Hill coefficient n_H were subsequently determined by fitting the calculated transformation yields Y to the modified Hill equation

$$Y([\mathrm{DNA}]) = Y(0) + (Y(\infty) - Y(0)) \cdot \frac{[\mathrm{DNA}]^{n_H}}{K_{1/2}^{n_H} + [\mathrm{DNA}]^{n_H}} \quad (1)$$

where $Y(0)$ and $Y(\infty)$ give the start and end points of the titration, respectively.

For determining the fraction of structures with unquenched fluorescence units in Fig. 5, we quantified the total number of structures in a TIRF image by counting the number of both weak (quenched) and bright (unquenched) red fluorescent spots. The fraction of red unquenched fluorescence units was then calculated as the fraction of the bright red spots of the total number of red spots. Because green quenched fluorescence units were not visible in TIRF images, the fraction of green unquenched fluorescence units was calculated by dividing the number of green spots by the total number of red spots and subsequently normalizing them by the fraction of colocalized red and green spots in fully transformed DNA origami arrays.

Statistical tests

Data and error bars are shown as the means and the 95% confidence interval, respectively. The transformation yield fractions were calculated from at least three TIRF images.

Supplementary Materials

The PDF file includes:
Supplementary Text
Figs. S1 to S18
Tables S1 to S12

Other Supplementary Material for this manuscript includes the following:
MDAR Reproducibility Checklist

REFERENCES AND NOTES

1. P. W. K. Rothemund, Folding DNA to create nanoscale shapes and patterns. *Nature* **440**, 297–302 (2006).
2. S. Dey, C. Fan, K. V. Gothelf, J. Li, C. Lin, L. Liu, N. Liu, M. A. D. Nijenhuis, B. Saccà, F. C. Simmel, H. Yan, P. Zhan, DNA origami. *Nat. Rev. Meth. Primers* **1**, 13 (2021).
3. A.-K. Pumm, W. Engelen, E. Kopperger, J. Isensee, M. Vogt, V. Kozina, M. Kube, M. N. Honemann, E. Bertosin, M. Langecker, R. Golestanian, F. C. Simmel, H. Dietz, A DNA origami rotary ratchet motor. *Nature* **607**, 492–498 (2022).
4. S. Li, Q. Jiang, S. Liu, Y. Zhang, Y. Tian, C. Song, J. Wang, Y. Zou, G. J. Anderson, J.-Y. Han, Y. Chang, Y. Liu, C. Zhang, L. Chen, G. Zhou, G. Nie, H. Yan, B. Ding, Y. Zhao, A DNA nanorobot functions as a cancer therapeutic in response to a molecular trigger in vivo. *Nat. Biotechnol.* **36**, 258–264 (2018).
5. J. Fu, Y. R. Yang, A. Johnson-Buck, M. Liu, Y. Liu, N. G. Walter, N. W. Woodbury, H. Yan, Multi-enzyme complexes on DNA scaffolds capable of substrate channelling with an artificial swinging arm. *Nat. Nanotechnol.* **9**, 531–536 (2014).
6. L. Grabenhorst, M. Pfeiffer, T. Schinkel, M. Kümmerlin, J. B. Maglic, G. A. Brüggenthies, F. Selbach, A. T. Murr, P. Tinnefeld, V. Glembockyte, Engineering modular and tunable single molecule sensors by decoupling sensing from signal output. *Nat. Nanotechnol.* **20**, 303–310 (2025).
7. S. M. Douglas, I. Bachelet, G. M. Church, A logic-gated nanorobot for targeted transport of molecular payloads. *Science* **335**, 831–834 (2012).
8. W. Engelen, C. Sigl, K. Kadletz, E. M. Willner, H. Dietz, Antigen-triggered logic-gating of DNA nanodevices. *J. Am. Chem. Soc.* **143**, 21630–21636 (2021).
9. S. Jia, H. Lv, Q. Li, C. Fan, F. Wang, DNA-based biocomputing circuits and their biomedical applications. *Nat. Rev. Bioeng.* **3**, 535–548 (2025).
10. S. Clamons, L. Qian, E. Winfree, Programming and simulating chemical reaction networks on a surface. *J. R. Soc. Interface* **17**, 20190790 (2020).
11. J. R. Burns, B. Lamarre, A. L. B. Pyne, J. E. Noble, M. G. Ryadnov, DNA origami inside-out viruses. *ACS Synthetic Biol.* **7**, 767–773 (2018).
12. A. E. Marras, Z. Shi, M. G. Lindell, R. A. Patton, C.-M. Huang, L. Zhou, H.-J. Su, G. Arya, C. E. Castro, Cation-activated avidity for rapid reconfiguration of DNA nanodevices. *ACS Nano* **12**, 9484–9494 (2018).
13. E. S. Andersen, M. Dong, M. M. Nielsen, K. Jahn, R. Subramani, W. Mamdouh, M. M. Golas, B. Sander, H. Stark, C. L. P. Oliveira, J. S. Pedersen, V. Birkedal, F. Besenbacher, K. V. Gothelf, J. Kjems, Self-assembly of a nanoscale DNA box with a controllable lid. *Nature* **459**, 73–76 (2009).
14. N. V. Voigt, T. Tørring, A. Rotaru, M. F. Jacobsen, J. B. Ravnsbaek, R. Subramani, W. Mamdouh, J. Kjems, A. Mokhir, F. Besenbacher, K. V. Gothelf, Single-molecule chemical reactions on DNA origami. *Nat. Nanotechnol.* **5**, 200–203 (2010).
15. Y. Wang, I. Baars, I. Berzina, I. Rocamonde-Lago, B. Shen, Y. Yang, M. Lolaico, J. Waldvogel, I. Smyrlaki, K. Zhu, R. A. Harris, B. Högberg, A DNA robotic switch with regulated autonomous display of cytotoxic ligand nanopatterns. *Nat. Nanotechnol.* **19**, 1366–1374 (2024).
16. F. Zhou, H. Ni, G. Zhu, L. Bershadsky, R. Sha, N. C. Seeman, P. M. Chaikin, Toward three-dimensional DNA industrial nanorobots. *Sci. Robot.* **8**, eadf1274 (2023).
17. J. Song, Z. Li, P. Wang, T. Meyer, C. Mao, Y. Ke, Reconfiguration of DNA molecular arrays driven by information relay. *Science* **357**, eaan3377 (2017).
18. D. Wang, J. Song, P. Wang, V. Pan, Y. Zhang, D. Cui, Y. Ke, Design and operation of reconfigurable two-dimensional DNA molecular arrays. *Nat. Protocols* **13**, 2312–2329 (2018).
19. Y. Cui, R. Chen, M. Kai, Y. Wang, Y. Mi, B. Wei, Versatile DNA origami nanostructures in simplified and modular designing framework. *ACS Nano* **11**, 8199–8206 (2017).
20. Y. Liu, H. Ge, Y. Wang, L. Tang, Y. Pei, S. Fan, Y. Song, C. Zhang, J. Song, Multistep transformations of DNA origami domino array via mechanical forces. *Small Struct.* **4**, 2200167 (2023).

21. Q. Yan, Y. Wang, J. Shi, B. Wei, Allostery of DNA nanostructures controlled by enzymatic modifications. *Nucleic Acids Res.* **48**, 7595–7600 (2020).
22. S. Fan, B. Ji, Y. Liu, K. Zou, Z. Tian, B. Dai, D. Cui, P. Zhang, Y. Ke, J. Song, Spatiotemporal control of molecular cascade reactions by a reconfigurable DNA origami domino array. *Angew. Chem. Int. Ed. Engl.* **61**, e202116324 (2022).
23. S. Fan, J. Cheng, Y. Liu, D. Wang, T. Luo, B. Dai, C. Zhang, D. Cui, Y. Ke, J. Song, Proximity-induced pattern operations in reconfigurable DNA origami domino array. *J. Am. Chem. Soc.* **142**, 14566–14573 (2020).
24. F. Cole, M. Pfeiffer, D. Wang, T. Schröder, Y. Ke, P. Tinnefeld, Controlled mechanochemical coupling of anti-junctions in DNA origami arrays. *Nat. Commun.* **15**, 7894 (2024).
25. H. Lv, N. Xie, M. Li, M. Dong, C. Sun, Q. Zhang, L. Zhao, J. Li, X. Zuo, H. Chen, F. Wang, C. Fan, DNA-based programmable gate arrays for general-purpose DNA computing. *Nature* **622**, 292–300 (2023).
26. R. Y. Lai, K. W. Plaxco, A. J. Heeger, Aptamer-based electrochemical detection of picomolar platelet-derived growth factor directly in blood serum. *Anal. Chem.* **79**, 229–233 (2007).
27. J. Andrae, R. Gallini, C. Betsholtz, Role of platelet-derived growth factors in physiology and medicine. *Genes Dev.* **22**, 1276–1312 (2008).
28. J. Bucci, P. Irmisch, E. Del Grosso, R. Seidel, F. Ricci, Timed pulses in DNA strand displacement reactions. *J. Am. Chem. Soc.* **145**, 20968–20974 (2023).
29. A. R. Chandrasekaran, Nuclease resistance of DNA nanostructures. *Nat. Rev. Chem.* **5**, 225–239 (2021).
30. M. Scheckenbach, T. Schubert, C. Forthmann, V. Glembockyte, P. Tinnefeld, Self-regeneration and self-healing in DNA origami nanostructures. *Angew. Chem. Int. Ed. Engl.* **60**, 4931–4938 (2021).
31. L. M. Wassermann, M. Scheckenbach, A. V. Baptist, V. Glembockyte, A. Heuer-Jungemann, Full site-specific addressability in DNA origami-templated silica nanostructures. *Adv. Mater.* **35**, e2212024 (2023).
32. S. M. Douglas, H. Dietz, T. Liedl, B. Högberg, F. Graf, W. M. Shih, Self-assembly of DNA into nanoscale three-dimensional shapes. *Nature* **459**, 414–418 (2009).
33. K. F. Wagenbauer, F. A. S. Engelhardt, E. Stahl, V. K. Hechtl, P. Stömmer, F. Seebacher, L. Meregalli, P. Ketterer, T. Gerling, H. Dietz, How we make DNA origami. *Chembiochem* **18**, 1873–1885 (2017).
34. T. Cordes, J. Vogelsang, P. Tinnefeld, On the mechanism of Trolox as antiblinking and antibleaching reagent. *J. Am. Chem. Soc.* **131**, 5018–5019 (2009).

Acknowledgments: We thank P. Luna, T. Charly, and P. Xaverl for their support with the measurements and A. Kardinal, K. Nazarbek Kyzy, F. Steger, and M. Ehrl for lab upkeep.
Funding: P.T. gratefully acknowledges financial support from the Federal Ministry of Education and Research (BMBF) in the framework of the Cluster4Future program (Cluster for Nucleic Acid Therapeutics Munich, CNATM) (Project ID: 03ZU1201AA) as well as the Free State of Bavaria under the Excellence Strategy of the Federal Government and the Länder through the ONE MUNICH Project Munich Multiscale Biofabrication. Y.K. acknowledges the support by Department of Energy grant DESC0020996, National Science Foundation grants CCF-2227399 and ECCS-2328217, and the National Institute of Health grants 1R35GM153472 and 1RM1GM145394. D.W. acknowledges the National Science Foundation of Jiangsu Province (BK20241817). M.P. acknowledges the support by Studienstiftung des Deutschen Volkes.
Author contributions: All authors conceived and developed the concept. M.P., F.C., and D.W. prepared samples and performed and analyzed the measurements. Y.K. and P.T. supervised the project. All authors have written, read, and approved the final manuscript. **Competing interests:** The authors declare that they have no competing interests. **Data and materials availability:** The experimental data generated in this study have been deposited in the Zenodo database: https://doi.org/10.5281/zenodo.15818028. Data supporting the findings of this manuscript are also available from the authors upon request.

Submitted 5 November 2024
Accepted 23 September 2025
Published 22 October 2025
10.1126/scirobotics.adu3679

Science Robotics

Spring-loaded DNA origami arrays as energy-supplied hardware for modular nanorobots

Martina Pfeiffer, Fiona Cole, Dongfang Wang, Yonggang Ke, and Philip Tinnefeld

Sci. Robot. **10** (107), eadu3679. DOI: 10.1126/scirobotics.adu3679

Science Robotics (ISSN 2470-9476) is published by the American Association for the Advancement of Science. 1200 New York Avenue NW, Washington, DC 20005. The title *Science Robotics* is a registered trademark of AAAS.